ORIGINAL PAPER

Benchmark reactive transport simulations of a column experiment in compacted bentonite with multispecies diffusion and explicit treatment of electrostatic effects

P. Alt-Epping · C. Tournassat · P. Rasouli · C. I. Steefel · K. U. Mayer · A. Jenni · U. Mäder · S. S. Sengor · R. Fernández

Abstract Bentonite clay is considered as a potential buffer and backfill material in subsurface repositories for high-level nuclear waste. As a result of its low permeability, transport of water and solutes in compacted bentonite is driven primarily by diffusion. Developing models for species transport in bentonite is complicated, because of the interaction of charged species and the negative surface charge of clay mineral surfaces. The effective diffusion coefficient of an ion in bentonite depends on the ion's polarity and valence, on the ionic strength of the solution, and on the bulk dry density of the bentonite. These dependencies need to be understood and incorporated into models if one wants to predict the effectiveness of bentonite as a barrier to radionuclides in a nuclear repository. In this work, we present a benchmark problem for reactive transport simulators based on a flow-through experiment carried out on a saturated bentonite core. The measured effluent composition shows the complex interplay of species transport in a charged medium in combination with sorption and mineral precipitation/dissolution reactions. The codes compared in this study are PHREEQC, CrunchFlow, FLOTRAN, and MIN3P. The benchmark problem is divided into four component problems of increasing complexity, leading up to the main problem which addresses the effects of advective and diffusive transport of ions through bentonite with explicit treatment of electrostatic effects. All codes show excellent agreement between results provided that the activity model, Debye-Hückel parameters, and thermodynamic data used in the simulations are consistent. A comparison of results using species-specific diffusion and uniform species diffusion reveals that simulated species concentrations in the effluent differ by less than 8 %, and that these differences vanish as the system approaches steady state.

P. Alt-Epping (✉) · A. Jenni · U. Mäder
Rock-Water Interaction Group, Institute of Geological Sciences, University of Bern, Baltzerstrasse 3, 3012 Bern, Switzerland
e-mail: alt-epping@geo.unibe.ch

C. Tournassat
BRGM, 45060 Orleans Cedex 2, France

P. Rasouli · K. U. Mayer
Department of Earth and Ocean Sciences, University of British Columbia, Vancouver, BC, Canada

C. I. Steefel
Lawrence Berkeley National Laboratory, Berkeley, CA, USA

S. S. Sengor
Southern Methodist University, Dallas, TX, USA

R. Fernández
Departamento de Geología y Geoquímica, Facultad de Ciencias, Universidad Autónoma de Madrid, Campus de Cantoblanco, 28049 Madrid, Spain

1 Introduction

Bentonite clay has been proposed as a potential buffer material in radioactive waste repositories so as to retain radionuclides and prevent their release into the biosphere. Common bentonite clays such as Wyoming MX-80 are composed primarily of Na-montmorillonite and typically contain quartz, aluminosilicates such as feldspars, gypsum, and calcite as accessory minerals. Bentonite is a suitable barrier material because of its swelling characteristics, sorption capacity, and anion repulsion. Swelling induces a very low hydraulic

conductivity such that transport of solutes in a compacted bentonite is driven primarily by diffusion. In bentonite research, much attention has been paid to describing the porosity structure and more recently to the electrostatic effects between the surfaces and interlayer space of montmorillonite and the solution and how these affect transport and the distribution of species in the pore space. Montmorillonite consists of tetrahedral-octahedral-tetrahedral (TOT) sheets and interlayers containing electrolyte between individual TOT layers (Fig. 1). The structure of these sheets results in an excess negative surface charge that generates layers of counter charge in the pore water near montmorillonite sheet surfaces. These layers may include ions adsorbed directly onto the sheet surface (Stern layer), as well as an electrical double layer (EDL) of largely immobile water containing excess cations adjacent to the negatively charged clay. Where the pore water is not affected by charged solid surfaces (i.e., "free or bulk water", Fig. 1), it is locally charge balanced.

Adding to the complexity of processes in bentonite systems is the fact that the distribution of the EDL and free water is dependent on the ionic strength of the free water and the bulk dry density of the bentonite. The thickness of the diffuse layer decreases with increasing ionic strength of the free water. Similarly, the volume fraction of free water decreases with increasing degree of compaction. A strongly compacted bentonite may not contain any free water at all.

The negative surface charge of montmorillonite attracts cations in the EDL, whereas anions are repelled. Anions therefore tend to be more abundant in the free pore water than in the EDL water. As a consequence, the pore space in which anions occur (i.e., the anion-accessible porosity) is smaller than in an uncharged clay with the same total porosity. This anion exclusion implies that the effective diffusion coefficient of anions cannot be characterized by a single diffusion coefficient and porosity value. Rather, it is a function of the physicochemical properties of the bentonite, the charge of the solute, and the pore solution. In highly compacted bentonite, the anion-accessible porosity may disappear altogether, resulting in an effective diffusion coefficient that is extremely low.

The porosity of a geological material is typically defined as the volume of voids over the total sample volume, and the pore water is the water contained within these voids. In contrast, in clay research, the term porosity and pore water is more ambiguous as the total porosity exhibits subdomains of distinct physicochemical properties. Conceptually, three types of porosities can be distinguished based on the
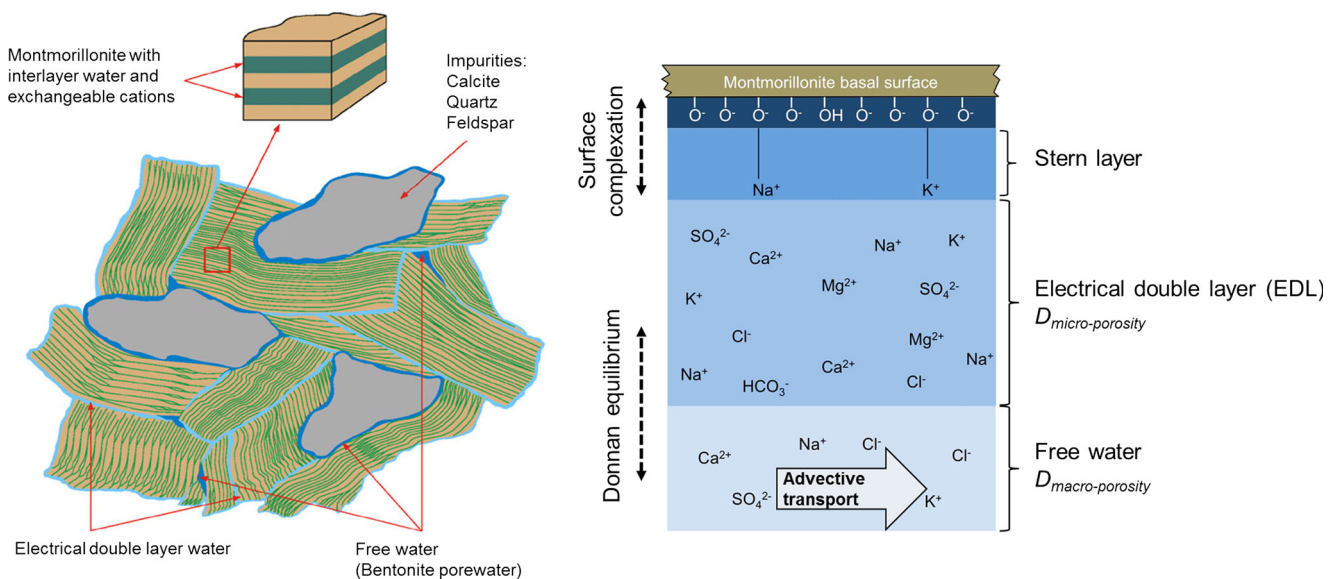
Fig. 1 Conceptual model of the types and distribution of pore water in bentonite. *Left panel* after Bradbury and Baeyens [21] and Tournassat and Appelo [4]. Montmorillonite crystals are made up of TOT layers containing interlayer water and exchangeable cations. The negative surface charge of montmorillonite induces an electrical field that attracts cations and repels anions. Thus, a diffuse or electrical double layer (EDL) with excess cations forms, which balances the surface charge of montmorillonite (*right panel*). Some ions are specifically adsorbed by the surface, forming a layer known as the Stern layer. Where electrostatic forces are not active, the pore space is filled with charge-balanced free (or bulk) water. While species in the free water are transported by advection and diffusion, species in the EDL are transported by diffusion only. Typically, diffusion in the EDL is orders of magnitudes slower than in the free water. In addition to diffusion within each layer, diffusive exchange may also occur between layers. Continuum models such as PHREEQC or CrunchFlowMC assume two different porosity domains, named the macroporosity and microporosity. The macroporosity contains free water, the microporosity, the diffuse or electrical double layer

characteristics of the pore water contained therein (Fig. 1): (1) the interlayer porosity is the space between individual TOT layers, filled with interlayer water which is strongly depleted in anions; (2) the microporosity containing the EDL with excess cations that balance the negative charge of the clay surface; and (3) the macroporosity containing free, charge-balanced pore water (e.g., [1–4]). The EDL and free pore water make up the interparticle porosity, comprising the space between individual mineral grains. Note that in the following discussion, the terms micro- and macroporosity are not defined in terms of a pore size distribution, but they are used to describe porosity subdomains, exhibiting distinct physicochemical properties.

Microstructural investigations of bentonite support this simplified multi-porosity concept in general, but there is evidence that the microstructure is more complex. For instance, Keller et al. [5] observed intergranular porosities (>10 nm) of about 5 and 0.1 vol% in bentonite with dry densities of 1.24 and 1.67 g/cm^3, respectively. At dry densities of 1.24 and 1.46 g/cm^3, intergranular pores were partly filled with clay aggregates forming a mesh-like structure. Within the cores of the structure, a low density material was found, presumably very fine clay similar to a colloid.

Since the properties of the bentonite are sensitive to changes in physicochemical conditions, ascribing a unique set of properties to bentonite becomes difficult. Not surprisingly, different mathematical models have emerged to describe the effects of the surface charge on the composition of the pore water and on solute transport. Birgersson and Karnland [6] developed a model that assumes a single type of porosity. The different transport characteristics of cations and anions are incorporated via an "ion equilibrium coefficient." However, the single porosity model tends to be accurate only for highly compacted bentonite and/or high ionic strengths of the pore water which led Tournassat and Appelo [4] to develop a more general approach involving multiple porosities to describe the distribution of surface charge, fluid composition, and transport processes.

At present, there are only a few continuum-based reactive transport codes that can handle transport of ions in a charged clay with explicit treatment of an EDL. In these codes, the interlayer space is considered to be part of the EDL. The total pore space is then divided into two porosity domains, the microporosity (i.e., the sum of interlayer space and the EDL) and the macroporosity containing free, charge-balanced water (Fig. 1, right panel). It is assumed that only the pore water in the macroporosity can move in response to a hydraulic gradient. Thus, in the macroporosity species, transport can occur by advection, dispersion, and diffusion, while in the microporosity, only diffusive transport takes place. This strict separation of mobile water within the macroporosity and stagnant water within the EDL is an approximation of reality as the EDL could be affected by advective flow as well.

Between these two porosity domains, diffusive exchange occurs, but presently, continuum codes such as PHREEQC [7] and CrunchFlowMC [8] assume that the transfer of mass between the microporosity and the macroporosity is instantaneous, consistent with a Donnan equilibrium between the two porosity domains (see Section 2.1 for details). A rigorous diffusion-controlled exchange has not yet been implemented into these codes. While the surface charge determines the distribution of counter charge in the EDL, the composition of the EDL is dependent on the exchange of ions with the free pore water. This dependence can be computed by assuming Donnan equilibrium (Section 2.1). This approach was incorporated into PHREEQC and subsequently applied by Appelo and Wersin [9]. A similar approach has been implemented into the code CrunchFlowMC.

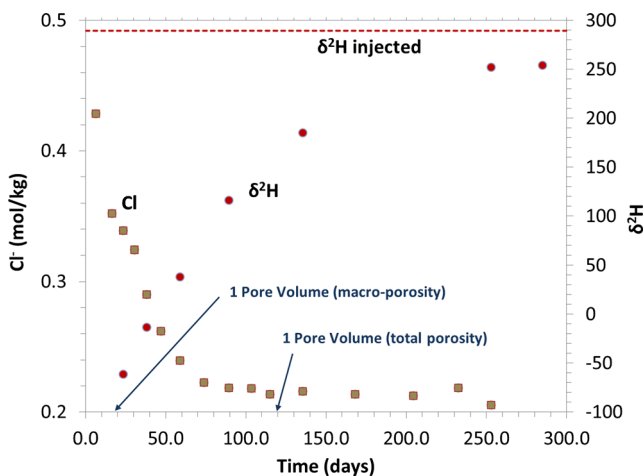### 1.1 The bentonite flow-through experiment

The benchmark problem is based on a multicomponent advective-diffusive column experiment carried out on a compacted bentonite core taken from a field experiment (LOT project) at Äspö, Sweden. The LOT project included multiple test series to examine the interaction between a bentonite buffer and a granitoid host rock in a repository-like environment. Field tests were carried out at elevated temperatures (with highest temperatures not exceeding 140 °C) to simulate heat generation from spent nuclear fuel [10]. Over the course of the 5-year field experiment, the bentonite remained compacted and fully saturated with in situ pore water.

The flow-through experiment was carried out at constant confining pressure and constant hydraulic gradient, resulting in a near-steady advective flux of 2.3e−9 m^3 m^{-2} s^{-1} [11, 12]. The temperature of the experiment changed slightly between 21 °C to just over 24 °C in winter and summer, respectively. Based on the measured water content, the total porosity of the bentonite was determined to be 47.6 %. From mass balance calculations, Fernández et al. [11] derived estimates for the micro- and macroporosity of 40.5 and 7.1 %, respectively. A synthetic pore water similar in composition to the natural pore water of the field experiment was injected into the column. The only significant differences between the initial and injected waters are a lower salinity (Na$^+$ and Cl$^-$) and a lower SO$_4^{2-}$ concentration in the infiltrating water. Deuterium was used as a tracer to monitor the breakthrough of the injected solution and to assess the degree of mixing between the initial pore water and the injected water.
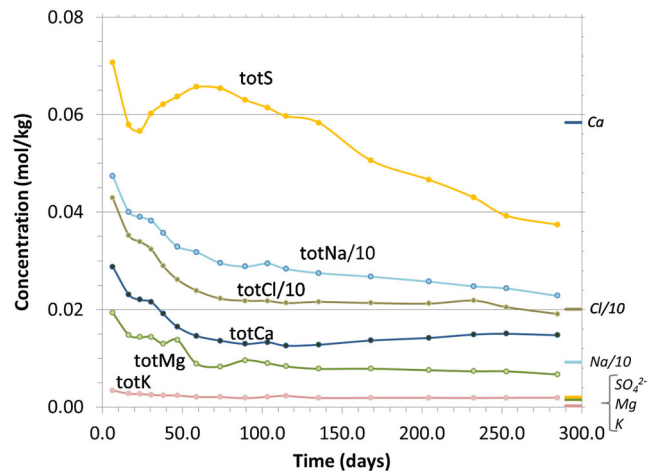
Monitoring the composition of the effluent during the experiment revealed the following:

1. The arrival of 50 % of the inlet deuterium (i.e., $0.5 \times (C_{inj} + C_{ini})$, where C_{inj} and C_{ini} refer to the injected and initial concentration, respectively) occurred after about 0.7 pore volumes if 1 pore volume is calculated from the total pore space of 47.6 %, or 5.0 pore volumes if calculated using the macroporosity value of 7.1 % (Fig. 2).

2. The displacement of the initial, more saline pore water with the more dilute injected fluid led to a decrease in Cl^- with time; the breakthrough of 50 % ($0.5 \times (C_{inj} + C_{ini})$) of the initial Cl^- concentration occurred after 0.2 pore volumes and about 1 pore volume, if 1 pore volume refers to the total porosity and to the macroporosity, respectively (Fig. 2).

3. Gypsum dissolution leads to an increase in SO_4^{2-} in the effluent and enhances the uptake of Ca^{2+} onto clay surfaces (Fig. 3).

4. The uptake of Ca^{2+} onto clay surfaces causes a release of Na^+, Mg^{2+}, and K^+ into solution (Fig. 3).

The rapid decrease in the Cl^- concentration in the effluent is consistent with the anion exclusion effect. As a result of the negative surface charge of montmorillonite, most of the Cl^- is located within the macroporosity, which makes up only a small fraction of the total porosity. As a consequence, Cl^- is rapidly flushed from the column. Cl^- is the only species attaining the inflow concentrations in the effluent

Fig. 3 Effluent composition during the first 300 days of the experiment. Shown on the right hand side are species concentrations in the infiltrating fluid. Compared to the composition of the injected fluid, the effluent shows a strong increase in SO_4^{2-}, a strong decrease in Ca^{2+} and a moderate increase in Na^+, Mg^{2+}, and K^+. The only species attaining the concentration of the infiltrating fluid is Cl^-. These compositional changes in the effluent are controlled by transport processes in combination with sorption and mineral reactions

within less than 300 days (Fig. 2). In contrast, deuterium is not only transported in the macroporosity but, because of its neutral charge, it also diffuses into the larger microporosity until both porosity domains have attained the same concentration. This leads to a stronger retardation of deuterium compared to Cl^-.

Deuterium and Cl^- behave conservatively and therefore illustrate the importance of electrostatic effects during transport of species through a compacted bentonite. The transport of all charged species in the system is affected by the electrostatic interaction with montmorillonite surfaces but, unlike Cl^- and ^2H, this interaction may occur in combination with other processes such as sorption and/or mineral dissolution/precipitation reactions. For instance, SO_4^{2-} concentrations are affected by the dissolution of gypsum and therefore increase over time. Similarly, the breakthrough of cations is affected by sorption and/or by mineral precipitation/dissolution reactions. The apparent inverse relationship between SO_4^{2-} and Ca^{2+} is an indication of a solubility control by gypsum in combination with the preferential sorption of Ca^{2+} onto montmorillonite surfaces in exchange for Na^+, Mg^{2+}, and K^+.

It should be noted that although the input and the design of this benchmark problem are based on a column experiment, this benchmark is not aimed at reproducing the outcome of the experiment in every detail. A more comprehensive description of the experiment, datasets, and a more detailed numerical model of the experiment will be presented in a forthcoming publication.

Fig. 2 Breakthrough curves for Cl^- and δ^2H. Flushing of the Cl^- in the initial pore water occurs relatively fast as Cl^- is transported by advection and diffusion through a fraction of the total porosity commonly referred to as the anion-accessible porosity. The uncharged tracer is transported through the macroporosity by advection and diffusion, but it also diffuses into the EDL, leading to a slower breakthrough compared to Cl^-. The breakthrough of the tracer is much slower and the effluent concentration never attains the concentration of the infiltrating fluid

2 Definition of the benchmark problems

The benchmark simulations are aimed at reproducing in qualitative terms the evolution of the effluent composition of the experiment for a given set of parameters. Furthermore, this benchmark compares species breakthrough curves for uniform and species-dependent effective diffusion coefficients so as to investigate the role of Fickian versus Nernst-Planck representations of diffusion [8, 13]. Different aspects of the system will be addressed in a step-wise approach by presenting four component problems of increasing complexity, leading finally to the main benchmark that includes an explicit treatment of EDL accumulation and transport (Table 1).

2.1 Multicomponent reactive transport model description

The computations presented below were carried out with the reactive transport codes CrunchFlow (and the Beta version CrunchFlowMC which includes explicit modelling of a diffuse layer) [8], PHREEQC V3 [7], a modified version of MIN3P ([14], Rasouli, unpublished), and FLOTRAN [15]. For short descriptions of the codes, the reader is also referred to Steefel et al. [8]. The governing equation for the conservation of solute mass in the free or macroporosity, ϕ^B, is given by Steefel et al. [8]:

$$\frac{\partial \left(\phi^B \Psi_j\right)}{\partial t} = \nabla \cdot \left(\phi^B D_j^* \nabla \Psi_j\right) - \nabla \cdot \left(\mathbf{q} \Psi_j\right) - \sum_{m=1}^{N_m} v_{jm} R_m, \tag{1}$$

where Ψ_j is the total concentration of the jth component or primary species defined by the following:

$$\Psi_j = C_j + \sum_{i=1}^{N_S} v_{ji} C_i + \sum_{k=1}^{N_X} v_{jk} C_k + \sum_{l=1}^{N_C} v_{jl} C_l, \tag{2}$$

where C_j is the concentration of a primary (or component) species in solution (in units of moles per m³ fluid). The total concentration includes N_S secondary aqueous species, C_i (considered as mobile), N_X exchanger species, C_k (considered as immobile), and N_C surface complexes, C_l (considered as immobile), while v_{ji}, v_{jk}, and v_{jl} are the corresponding aqueous, exchanger, and surface complexes stoichiometric coefficients, respectively. The reaction term in Eq. 1 consists of N_m mineral reactions, R_m, all considered as kinetically controlled. Here, $\mathbf{q}$ is the Darcy flux, D_j^* is the pore diffusion coefficient of the jth species, ϕ is the porosity, and v_{jm} is the stoichiometric coefficient for mineral reactions. The effective diffusion coefficient D_j, the pore diffusion coefficient, and the diffusion coefficient in water D_j^0 are related via the porosity and the tortuosity τ by

$$D_j = \phi D_j^* = \phi \tau D_j^0. \tag{3}$$

The corresponding governing equation for the EDL porosity is given by the following:

$$\frac{\partial \left(\phi^{EDL} \Psi_j^{EDL}\right)}{\partial t} = \nabla \cdot \left(\phi^{EDL} D_j^{EDL*} \nabla \Psi_j^{EDL}\right), \tag{4}$$

where ϕ^{EDL} is the EDL porosity, Ψ_j^{EDL} is the total concentration in the EDL, and D_j^{EDL*} is the pore diffusion coefficient (which may be species-specific) in the EDL. Mineral-water reactions are assumed to take place in the macroporosity, while transport within the EDL is assumed to be purely diffusive (no flow).

Mineral dissolution-precipitation reactions are formulated as kinetic reactions according to the following general rate expression:

$$R_m = -A_m k_m \left[1 - \frac{Q_m}{K_m}\right], \tag{5}$$

Table 1 Summary of the component benchmark problems leading up to the main problem in step 5

	Step	Problem	Diffusion	Surface reaction
Component benchmark				
	1	Non-reactive transport	Fickian	
			Nernst-Planck	
	2	Reactive transport involving implementation of reaction network	Fickian	
			Nernst-Planck	
	3	"Conventional" ion-exchange on montmorillonite surfaces	Fickian	Ion exchange
			Nernst-Planck	
	4	Implementation of an EDL induced by charged montmorillonite surfaces	Nernst-Planck	EDL
Main	5	Component problem 4 in combination with surface complexation representing a Stern layer	Nernst-Planck	EDL, Surface complexation

where k_m is the far from equilibrium dissolution rate at the temperature of interest (25 °C), A_m is the mineral reactive surface area in the rock matrix, Q_m is the ion activity product, and K_m is the equilibrium constant for the mineral dissolution reaction.

We use a simplified approach to represent the hydraulic aspects of the experiment. Rather than imposing a pressure gradient over the length of the column as was done in the experiment, we assume a constant Darcy flux **q** of 2.3e−9 m³ m⁻² s⁻¹. Hydrodynamic dispersion is ignored. Molecular diffusion is usually described in terms of Fick's First Law as

$$J_j = -D_j \nabla C_j, \tag{6}$$

where J_j is the diffusive flux. Equation 6 does not account for electrostatic forces induced by species of nonzero charge, and it is therefore strictly valid only for uncharged species. Steefel and Maher [13] pointed out that even in steady-state systems, the use of a single diffusion coefficient may present problems. However, in some cases, a single diffusion coefficient may be used for a specific system (generally at least pH dependent), as discussed by Molins et al. [16]. The simplification of using a single diffusion coefficient offers the advantage that local charge balance is guaranteed and charge-induced electrostatic interaction is avoided which simplifies numerical execution. The disadvantage is that species properties such as ion size, charge, and hydration energy which may affect species-specific diffusivities are ignored [17].

Rigorous modelling of diffusion in systems containing charged species requires electrochemical migration to be included as a transport process in such a way that positively and negatively charged species move in a coordinated manner to maintain local charge balance. The diffusion of species j then depends on the concentration gradient of itself and other charged species. Formulations for multispecies diffusion are commonly based on the Nernst-Planck equation (e.g., [8, 13]):

$$J_j = -D_j \nabla C_j - \frac{D_j C_j}{RT} z_j F \nabla \varphi, \tag{7}$$

where z_j is the charge of species j; F and R are the Faraday and gas constants, respectively; T is the temperature; and φ is the electrical potential. The Nernst-Planck equation describes the flux of ions driven by a concentration gradient and the electrical field created by the movement of different ions.

PHREEQC and CrunchFlowMC have implemented a Donnan approach to describe the electrical potential and species distribution in the EDL. This approach implies a uniform electrical potential φ^{EDL} in the EDL and an instantaneous equilibrium distribution of species between the EDL and the free water (i.e., between the micro- and

macroporosity, respectively). The assumption of instantaneous equilibrium implies that diffusion between micro- and macroporosity is not considered explicitly and that at all times the chemical potentials, μ_i, of the species are the same in the two porosities:

$$\mu_i^{EDL} = \mu_i^B. \tag{8}$$

The distribution of species in the two porosity domains can be written as follows:

$$C_i^{EDL} = C_i^B \exp\left(\frac{-z_i e \varphi^{EDL}}{k_B T}\right), \tag{9}$$

where C_i^{EDL} and C_i^B are the concentrations in the micro- and macroporosity, respectively; e is the elementary charge; z_i is the valence of species i; k_B is the Boltzmann constant; T is the absolute temperature; and φ^{EDL} is the mean electrical potential in the microporosity.

Unlike the charge-balanced solution in the macroporosity, the solution in the microporosity exhibits a net charge which balances the total charge of the montmorillonite surfaces, that is.

$$\phi^{EDL} \sum_i z_i C_i^{EDL} = Q_{SL}, \tag{10}$$

where Q_{SL} is the total surface charge.

To determine the volume of the microporosity, the surface area of montmorillonite, and the Debye length, D_L, which is the distance from the charged mineral surface to the point where electrical potential decays by a factor of e, needs to be known. The volume of the microporosity can then be calculated as

$$\phi^{EDL} = A_{clay} D_L, \tag{11}$$

where A_{clay} is the charged surface area of the clay mineral. The Debye length is a function of temperature and the ionic strength of the free water in the macroporosity:

$$D_L = \frac{\beta_D}{\sqrt{I}}, \tag{12}$$

where β_D is a temperature dependent factor (3 ×10⁻¹⁰ at 25 °C) and I is the ionic strength of the free water. In this benchmark problem, the Debye length is assumed to remain constant. This assumption was made because of code limitations at the time when the benchmark simulations were carried out.

3 Detailed problem specification

3.1 Flow and transport model specification

The model column has a length of 0.05 m and is discretized into 25 cells. We assume a unit cross-sectional area. The

total duration of the experiment is 300 days. The temperature of the model experiment is assumed to be constant at 25 °C, which is slightly higher than the actual temperatures in the laboratory experiment (Section 1.1). A constant influx of $2.3e-9$ m^3 m^{-2} s^{-1} is assigned to the left-hand boundary. Hydrodynamic dispersion is neglected and thus dispersivity is set to zero. Material properties are uniform throughout the column.

In component problems 1–3, the porosity is 7.1 %. Each of the component problems 1–3 includes two sub-scenarios, one involving a uniform diffusion coefficient of $1.87e-9$ m^2 s^{-1} for all species, the other species-specific diffusion coefficients (Table 2). In component problems 4 and 5, which include the implementation of an explicit EDL model, only species-dependent diffusion coefficients are used. Species-specific diffusion coefficients in the macroporosity were derived from the ionic mobility in free water at 25 °C [18, 19]. For all species without a specific diffusion coefficient, a diffusion coefficient of $1.87e-9$ m^2 s^{-1} is used.

Diffusion in the EDL is assumed to be negligible and species-specific diffusion coefficients of cations listed in Table 2 are assumed to be an arbitrary 3 orders of magnitude lower than those in free water. A diffusion coefficient of $1e-16$ m^2 s^{-1} is assigned to the anions Cl^-, SO_4^{2-}, and HCO_3^-. All remaining species have a diffusion coefficient of $1.87e-12$ m^2 s^{-1}. Note that different codes may handle transport of species in the EDL differently. For instance, CrunchFlow reads diffusion coefficients for all species in the EDL, while PHREEQC uses the viscosity of the EDL pore water to control species transport. The benchmark problems involving an EDL (component problems 4 and 5) only require that diffusion within the EDL is negligible. We assume that molecular and pore diffusion coefficients are identical (i.e., tortuosity $\tau = 1$) and the effective diffusion coefficient is computed from Eq. 3.

3.2 Reaction network description

3.2.1 Chemical system (components, complexes, gases, minerals)

The chemical system with component species, secondary species, and minerals, including their dissociation reactions and thermodynamic constants are summarized in Tables 3, 4, and 5, respectively. Activity coefficients are calculated according to the extended Debye-Hückel equation given by the following:

$$\ln \gamma_i = -A z_i^2 \frac{\sqrt{I}}{1 + B a_i \sqrt{I}} + \beta_i I, \qquad (13)$$

where the hard core diameter of each aqueous species a_i is listed in Table 4 and the Debye-Hückel parameters A, B, and β of all species are as follows:

A	B	β_i(charged)	β_i(uncharged)
0.5114	0.3288	0.041	0.1

Consistency of thermodynamic data for minerals and aqueous species and of activity coefficients for aqueous species are important to obtain a good agreement between codes which may in some cases involve slight modifications of the default versions of codes and/or their thermodynamic databases. For instance, codes such as FLOTRAN or CrunchFlow read thermodynamic constants at discrete temperatures from a database and use an interpolation function to calculate the equilibrium constants for intermediate temperatures. The user needs to make sure that the interpolated equilibrium constants agree with the constants listed in Tables 4 and 5.

Table 2 Diffusion coefficients of species in free water

Species name	D (free water), m^2 s^{-1}
H^+	$8.57e-9$
Ca^{2+}	$7.9e-10$
Mg^{2+}	$7.0e-10$
K^+	$1.96e-9$
Na^+	$1.33e-9$
Cl^-	$2.03e-9$
SiO_2,aq	$1.0e-9$
Al^{3+}	$5.14e-10$
SO_4^{2-}	$1.06e-9$
HCO_3^-	$1.18e-9$
Tracer (^{2}H)	$1.87e-9$

Table 3 List of components, secondary species, minerals, and gases

Component species
H^+
Ca^{2+}
Mg^{2+}
K^+
Na^+
Cl^-
SiO_2,aq
Al^{3+}
SO_4^{2-}
HCO_3^-
^{2}H

Table 4 Properties of component species and secondary species

Species name		$\log K$ (25 °C)	Hard core diameter (a_i)
H^+	H^+	0	9.0
Ca^{2+}	Ca^{2+}	0	6.0
Mg^{2+}	Mg^{2+}	0	8.0
K^+	K^+	0	3.0
Na^+	Na^+	0	4.0
Cl^-	Cl^-	0	3.0
SiO_2,aq	SiO_2,aq	0	3.0
Al^{3+}	Al^{3+}	0	9.0
SO_4^{2-}	SO_4^{2-}	0	4.0
HCO_3^-	HCO_3^-	0	4.0
OH^-	$+ H^+ = H_2O$	13.9951	3.5
$Al(OH)_2^+$	$+2 H^+ = Al^{3+} + 2 H_2O$	10.5945	4.0
AlO_2^-	$+4 H^+ = Al^{3+} + 2 H_2O$	22.8833	4.0
$AlOH^{2+}$	$+ H^+ = Al^{3+} + H_2O$	4.9571	4.5
$HAlO_2(aq)$	$+3 H^+ = Al^{3+} + 2 H_2O$	16.4329	3.0
$CaCl^+$	$= Ca^{2+} + Cl^-$	0.6956	4.0
$CaCl_2(aq)$	$= Ca^{2+} + 2 Cl^-$	0.6436	3.0
$CaSO_4(aq)$	$= Ca^{2+} + SO_4^{2-}$	−2.1111	3.0
$CaCO_3(aq)$	$+ H^+ = Ca^{2+} + HCO_3^-$	7.0017	3.0
$CaHCO_3^+$	$= Ca^{2+} + HCO_3^-$	−1.0467	4.0
$CaHSiO_3^+$	$+ H^+ = Ca^{2+} + SiO_2(aq) + H_2O$	8.576	4.0
$CaOH^+$	$+ H^+ = Ca^{2+} + H_2O$	12.833	4.0
CO_3^{2-}	$+ H^+ = HCO_3^-$	10.3288	4.5
$CO_2(aq)$	$+ H_2O = H^+ + HCO_3^-$	−6.3447	3.0
$KCl(aq)$	$= K^+ + Cl^-$	1.4946	3.0
KSO_4^-	$= K^+ + SO_4^{2-}$	−0.8796	4.0
$KOH(aq)$	$+ H^+ = H_2O + K^+$	14.439	3.0
$MgCl^+$	$= Mg^{2+} + Cl^-$	0.1349	4.0
$MgSO_4(aq)$	$= Mg^{2+} + SO_4^{2-}$	−2.4117	3.0
$MgCO_3(aq)$	$+ H^+ = Mg^{2+} + HCO_3^-$	7.3499	3.0
$MgHCO_3^+$	$= Mg^{2+} + HCO_3^-$	−1.0357	4.0
$MgOH^+$	$+ H^+ = Mg^{2+} + H_2O$	11.682	3.0
$NaCl(aq)$	$= Na^+ + Cl^-$	0.7770	3.0
$NaSO_4^-$	$= Na^+ + SO_4^{2-}$	−0.70	4.0
$NaHSiO_3(aq)$	$+ H^+ = H_2O + Na^+ + SiO_2(aq)$	7.755	3.0
$NaOH(aq)$	$+ H^+ = Na^+ + H_2O$	14.205	3.0
$NaCO_3^-$	$+ H^+ = Na^+ + HCO_3^-$	9.8144	4.0
$NaHCO_3(aq)$	$= Na^+ + HCO_3^-$	−0.1541	3.0
$NaAlO_2(aq)$	$+4 H^+ = Al^{3+} + Na^+ + 2 H_2O$	23.6266	3.0
$H_2SiO_4^{2-}$	$+2 H^+ = SiO_2(aq) + 2 H_2O$	23.00	4.0
$HSiO_3^-$	$+ H^+ = H_2O + SiO_2(aq)$	9.9525	4.0
$HCl(aq)$	$= H^+ + Cl^-$	−0.67	3.0

3.2.2 Chemical conditions

Two chemical conditions are specified, one for the infiltrating fluid to be used as the inflow boundary condition, the other for the initial mineralogy and pore-water compositio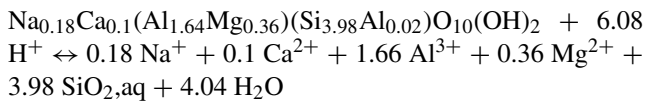n of the bentonite (Table 6). Flux-type (zero-gradient) boundary conditions are applied to the inflow and outflow boundaries. The initial composition of the bentonite pore water was derived by Fernández et al. [11] based on the measured composition of exchange sites and the assumption of initial gypsum and calcite equilibrium.

Table 5 Minerals

Mineral name		$\log K$ (25 °C)	V_m (cm^3 mol^{-1})
Calcite	$CaCO_3 + H^+ = Ca^{2+} + HCO_3^-$	1.8487	36.934
Gypsum	$CaSO_4 = Ca^{2+} + SO_4^{2-}$	−4.4823	74.69
Quartz	$SiO_2 = SiO_2(aq)$	−3.9993	22.688
K-feldspar	$KAlSi_3O_8 + 4\ H^+ = K^+ + Al^{3+} + 3\ SiO_2(aq) + 2\ H_2O$	−0.2753	108.87
MX-80	See below	5.9941	134.88

Initial mineral volume fractions and kinetic parameters of minerals are summarized in Table 7. Montmorillonite is the only sorbent in the system. Although it is assumed to be nonreactive and can be treated as a generic exchanger, Fernández et al. [11] defined its stoichiometry and dissociation reaction as follows:

$Na_{0.18}Ca_{0.1}(Al_{1.64}Mg_{0.36})(Si_{3.98}Al_{0.02})O_{10}(OH)_2 + 6.08\ H^+ \leftrightarrow 0.18\ Na^+ + 0.1\ Ca^{2+} + 1.66\ Al^{3+} + 0.36\ Mg^{2+} + 3.98\ SiO_2,aq + 4.04\ H_2O$

Montmorillonite has a molar volume and weight of 134.88 and 368.44 g mol^{-1}, respectively, yielding a density of 2.731 kg l^{-1}. The total exchange capacity of montmorillonite (CEC) is fixed at 73.66 meq/100 g$_{bulk\_dry\_rock}$. The bentonite has a bulk dry density of 1.4 kg l^{-1}, while a specific surface area of 788 m^2 g$^{-1}_{mineral}$ is assumed [20].

Selectivity coefficients for the benchmark scenario involving classic ion exchange (component problem 3) are taken from Bradbury and Baeyens [21] and are summarized in Table 8. The Gaines-Thomas convention to calculate exchanger activities is adopted.

In the main problem (component problem 5), 10 % of the total charge is compensated in a Stern layer (Fig. 1, right panel). The percentage of charge compensated in the Stern layer is assumed to remain constant irrespective of changes in the ionic strength. Conceptually, this scenario represents a system in which 10 % of the charge is carried by surfaces that are not in contact with the pores through which advective and/or diffusive transport occurs. In other words, 10 % of the charge is present in "interlayer-like" pores with surfaces undergoing cation exchange, while 90 % of the charge is compensated by the diffuse layer developing on surfaces in contact with larger pores. In simulations with Crunch-FlowMC presented below, 90 % of the charge is assigned to a so-called fixed mineral charge, while 10 % is assigned to a surface undergoing surface complexation according to parameters given in Table 9. The very low surface complexation constant of the first surface complexation reaction in Table 9 ensures that all surface sites undergoing surface complexation are occupied by cations. This implies that the concentration of free *montmor*$^-$ sites is zero, and that for this particular surface type, the charge balance contribution from the EDL is also zero [22]. The remaining surface complexation constants are set to be consistent with cation exchange selectivity coefficients in Table 8. In simulations with PHREEQC, we consider that 10 % of the charge is carried by the exchanger analogue to component problem 3, while the remaining 90 % corresponds to a surface undergoing no surface complexation. These two slightly different approaches are dictated by the definition of the benchmark problem and by the structure and surface definitions in the two codes. Because over the course of the experiment the

Table 6 Total component concentrations and constraints of the infiltrating fluid (inflow) and the initial pore water (initial)

Species name	Inflow (mol kg^{-1})	Constraint	Initial (mol kg^{-1})	Constraint
pH	7.2		8.5	
Ca^{2+}	0.0584		0.035	
Mg^{2+}	1.52e−3		0.025	
K^+	2.5e−4		0.005	
Na^+	0.092		0.464	Charge balance
Cl^-	0.208	Charge balance	0.5	
SiO_2,aq	1e−5		1e−5	
Al^{+3}	1e−8		1e−5	
SO_4^{2-}	2.02e−3		0.0442	Gypsum eq.
HCO_3	1.2e−4		7.153e−5	Calcite eq.
Tracer (^{2}H)	0.200		0.1433	

Table 7 Mineralogy and mineral kinetic properties

Mineral name	Volume fraction	Log rate constant, mol m^{-2} s^{-1}	Reactive surface area
Calcite	0.0036	−6.19	100 (m^2 m$^{-3}_{bulk}$)
Gypsum	0.0086	−3	100 (m^2 m$^{-3}_{bulk}$)
Quartz	0.0521	−13.39	100 (m^2 m$^{-3}_{bulk}$)
K-feldspar	0.0809	−13	100 (m^2 m$^{-3}_{bulk}$)
MX-80	0.3786	−50	788 (m^2 g$^{-1}_{mineral}$)

pH of the pore water did not change significantly, protonation/deprotonation reactions on montmorillonite edge sites are neglected.

4 Output specification

The simulation output includes in all benchmark scenarios the breakthrough curves of total species concentrations at the outlet of the column (i.e., cell number 25) over a period of 300 days. In component problems 1–3, the percent deviation, %D, of species concentrations using species-specific diffusion (C_{MCD}) from concentrations using a single diffusion coefficient (C_{SD}) are evaluated according to the following expression:

$$\%D = \frac{|C_{MCD} - C_{SD}|}{C_{SD}} \times 100 \qquad (14)$$

The output in component problem 3 includes the composition of the exchange sites in moles per liter$_{bulk}$. The output in component problems 4 includes the spatial profile of the composition of the EDL in molality, and in component problem 5, the spatial profile of the composition of the Stern layer in moles per liter$_{bulk}$ after 300 days. Furthermore, in component problem 4, we evaluate the effect of anion exclusion by comparing the breakthrough of deuterium and Cl$^-$ in the last cell of the model domain with and without implementation of an EDL. The deuterium concentration is given in δ^2H(‰). The tracer in Table 6 represents the

hydrogen isotope ratio ^{2}H/^{1}H. Although the concentration of the tracer is in molality, it is numerically equivalent to ^{2}H/^{1}H in part per million. Ignoring the inconsistency in units, the conversion to the required output format is as follows:

$$\delta^2 H(‰) = \frac{\left([\text{Tracer}] \times 1000 - \frac{^2H}{^1H}(\text{VSMOW})\right) \times 1000}{\frac{^2H}{^1H}(\text{VSMOW})} \qquad (15)$$
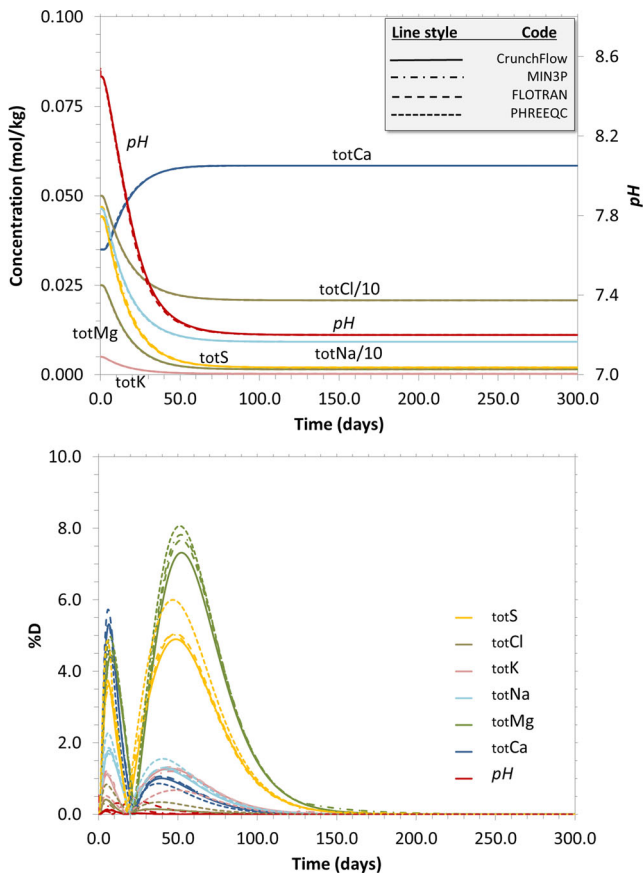
where $\frac{^2H}{^1H}$(VSMOW) = 155.76 ppm

5 Component simulations

5.1 Simulation of transport only

The first component problem involves transport of all components and complexes through the column without mineral reaction or sorption. A uniform porosity of 0.071 and a constant flux of 2.3e−9 m^3 m^{-2} s^{-1} are assumed. This component problem assesses the difference between a Fickian and a Nernst-Planck representation of diffusion according to Eq. 14. Results of this component problem are summarized in Fig. 4.

Table 9 Surface complexation reactions representing the Stern layer in component problem 5. Note that a log$K = -30$ of the first reaction ensures that all surface sites *montmor*$^-$ (making up 10 % of the total surface charge) are occupied by cations. Thus, only 90 % of the total surface charge is balanced by the EDL [22]. This approach is equivalent to the ion exchange reactions in component problem 3

Surface complexation (benchmark 5)	log$K$
Na-*montmor* =Na$^+$+*montmor*$^-$	−30
Ca-*montmor*$_2$+2 Na$^+$ =Ca^{2+}+2 Na-*montmor*	−0.41
K-*montmor* +Na$^+$ =K$^+$+Na-*montmor*	−0.60
Mg-*montmor*$_2$+2 Na$^+$ =Mg^{2+}+2 Na-*montmor*	−0.34

Table 8 Selectivity coefficients for ion exchange reactions

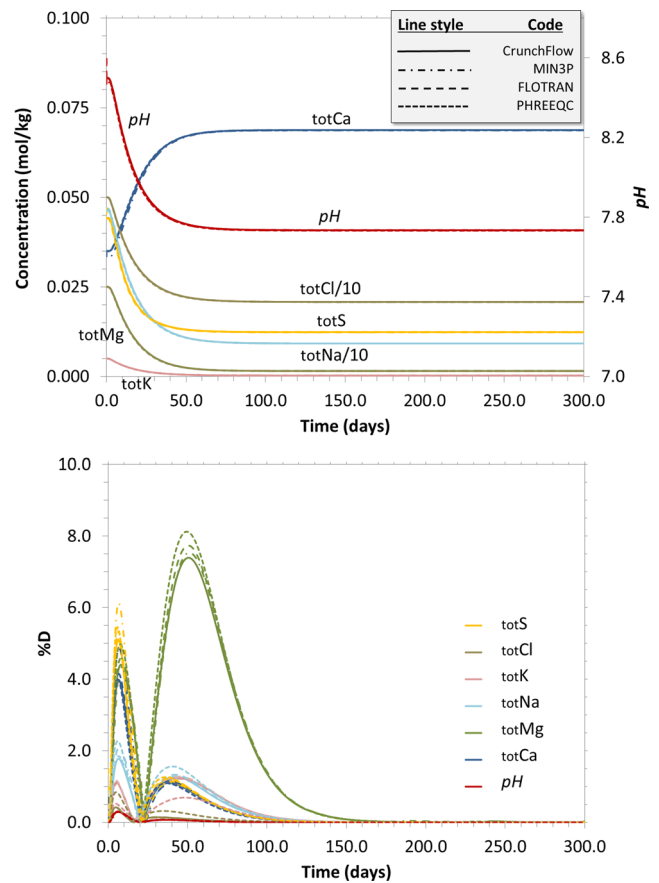| Exchange reaction (benchmark 3)	Ks
Na$^+$ + *montmor*$^-$ = Na-*montmor*	1.0
Na-*montmor* + K$^+$ = K-*montmor* + Na$^+$	4.0
2 Na-*montmor* + Mg^{2+} = Mg-*montmor*$_2$ + 2 Na$^+$	2.2
2 Na-*montmor* + Ca^{2+} = Ca-*montmor*$_2$ + 2 Na$^+$	2.6

Fig. 4 Results of component problem 1. The *upper panel* shows the composition of the pore water in cell number 25 versus time for species dependent diffusion. The *lower panel* shows the %D between uniform (Fickian) and species-dependent (Nernst-Planck) diffusion. The Mg^{2+} concentration shows the largest difference between the two diffusion scenarios. The system attains steady state at about 150 days (*upper panel*). After this time, there is no difference between uniform and species-dependent diffusion. Although all codes used in this component benchmark problem generally show very good agreement between the breakthrough curves for Fickian and Nernst-Planck-based diffusion, in calculations with PHREEQC, the %D evolution slightly deviates from that of the other codes between 0–100 days (*lower panel*). For instance, the %D of SO_4^{2-} after 50 days exceeds the %D of the other codes by about 1 %
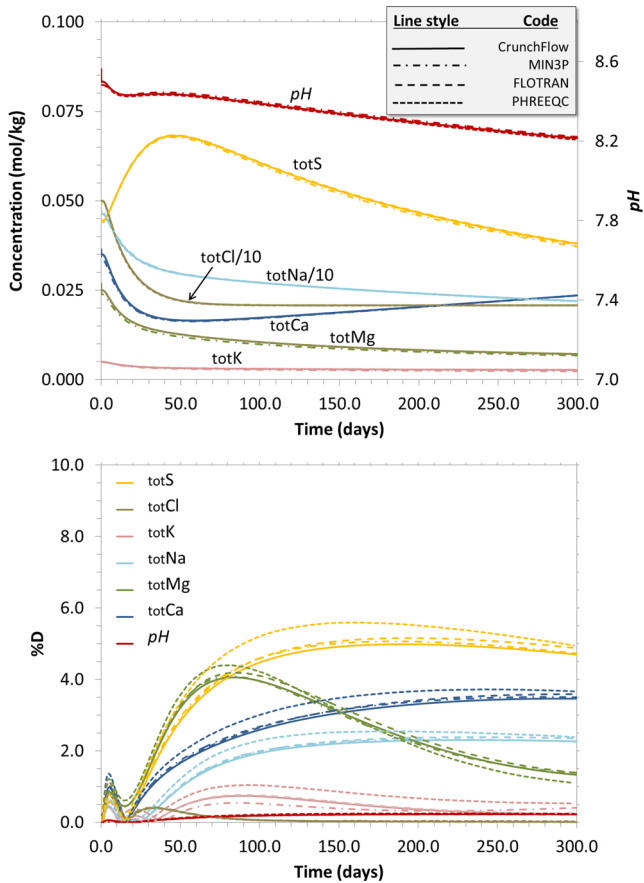
Fig. 5 Results of component problem 2. The *upper panel* shows the composition of the pore water in cell number 25 versus time for species dependent diffusion. Adding gypsum to the system results in overall higher Ca^{2+} and SO_4^{2-} concentrations than in component problem 1 (Fig. 4, *upper panel*). However, the Ca^{2+} concentration exceeds the SO_4^{2-} concentration, which is not consistent with observations from the experiment (Fig. 3). The lower panel shows the %D between uniform (Fickian) and species-dependent (Nernst-Planck) diffusion. The Mg^{2+} concentration shows the largest difference between the two diffusion scenarios. The system attains steady state at about 150 days (*upper panel*). After this time, there is no difference between uniform and species-dependent diffusion. Similar to component problem 1, all codes used in this component benchmark problem generally show very good agreement between the breakthrough curves for Fickian and Nernst-Planck-based diffusion. However, in calculations with PHREEQC, the %D of some species tends to slightly deviate from that computed with the other codes between 0–100 days (*lower panel*). Buffering by gypsum dissolution leads to a better match in the %D of SO_4^{2-} than in Fig. 4, *lower panel*

5.2 Implementing the reaction network, no surface reaction

This component problem includes the entire reaction network (Tables 2–7), but surface reactions (cation exchange, surface complexation, and the formation of the EDL) are not yet considered. A uniform porosity of 0.071 and a constant flux of 2.3e−9 m^3 m^{-2} s^{-1} are assumed.

This simulation scenario includes a comparison of a Fickian and a Nernst-Planck formulation of diffusion. Results of this component problem are shown in Fig. 5.

### 5.3 Adding conventional ion exchange

This simulation builds on component problem 2, but considers "conventional" ion exchange reactions (i.e., sorption on permanently charged cation exchange sites as opposed to surface complexation involving pH-dependent sorption on

variably charged surfaces). Selectivity coefficients for ion exchange reactions are listed in Table 8. The CEC and other properties of montmorillonite are given in Section 3.2.2. A single porosity of 0.071 is assumed.

This component problem also involves a comparison between a Fickian and a Nernst-Planck representation of diffusion. Results of this component benchmark are summarized in Figs. 6 and 7.


Fig. 6 Results of component problem 3. The *upper panel* shows species breakthrough curves in the last cell of the column for species dependent diffusion. Gypsum dissolution in combination with ion exchange yields SO_4^{2-} concentrations exceeding Ca^{2+} concentrations. After an initial decrease, the Ca^{2+} concentration increases as with time the exchange sites become progressively occupied with Ca^{2+} such that less Ca^{2+} moves onto the exchanger. This leads to a decrease in SO_4^{2-} which is consistent with a solubility control by gypsum and is consistent with observations from the experiment (Fig. 3). The *lower panel* shows the %D between Fickian and Nernst-Planck formulations of diffusion. All codes used in this component benchmark problem generally show very good agreement between the breakthrough curves for Fickian and Nernst-Planck-based diffusion. However, the %D tends to be slightly higher in calculations with PHREEQC compared to the other codes (*lower panel*)
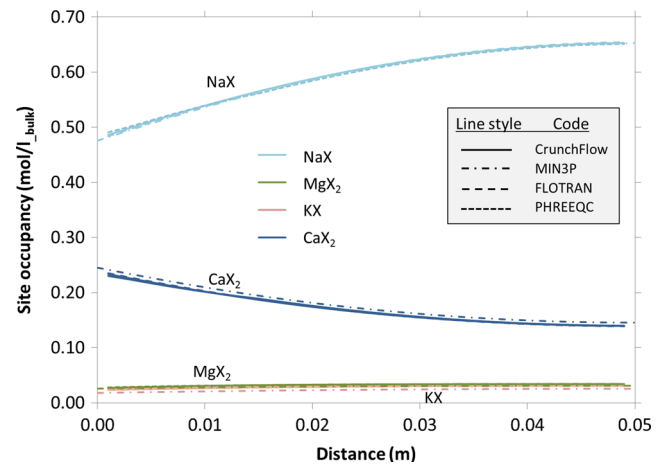

Fig. 7 Spatial profile along the column of the site occupancy on montmorillonite surfaces. The profiles reflect the preferred uptake of Ca^{2+} onto the exchanger leading to the release of Na^+, Mg^{2+}, and K^+ into the pore water

5.4 Implementation of an EDL

This scenario involves the implementation of species-specific diffusion according to Table 2 and an EDL that compensates the surface charge of montmorillonite. The total porosity amounts to 47.6 % which is divided into 40.5 % microporosity (EDL) and 7.1 % macroporosity (free water). From the microporosity and the surface area of montmorillonite (Table 7), the Debye length of the EDL calculated from Eq. 11 is 4.97e−10 m. The Debye length
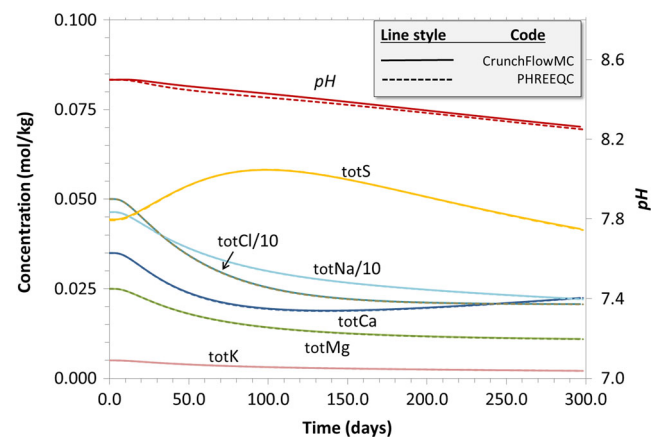
Fig. 8 Results for component problem 4 showing the composition of the pore water in cell number 25 versus time. Both codes show excellent agreement between breakthrough curves except for a slight discrepancy in pH
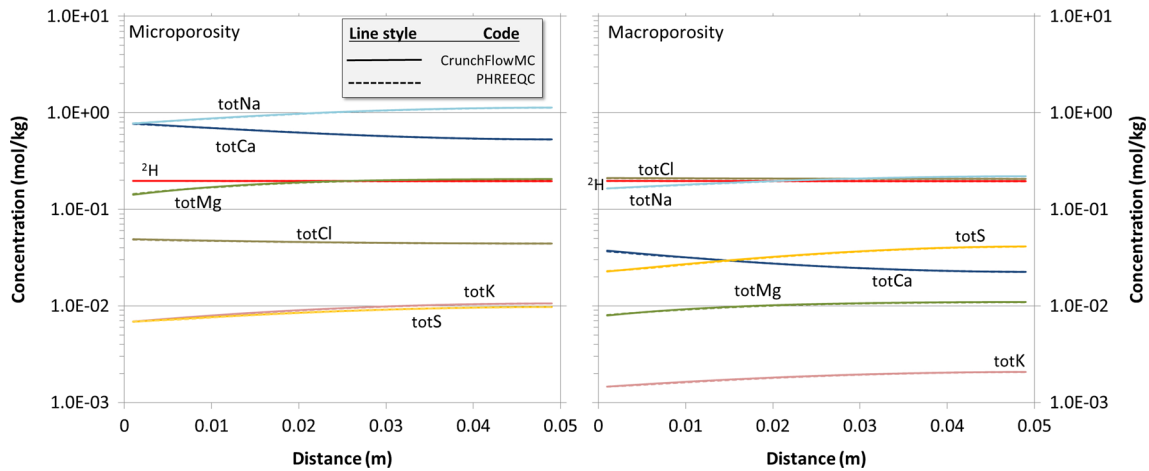
Fig. 9 Spatial profiles of the porewater composition in the micro- and macroporosity (*left and right panels*, respectively) after 300 days. Donnan equilibrium is assumed between the two porosity domains. Unlike conventional ion exchange, the negatively charged surface of montmorillonite affects the distribution of anions in the pore space.

Negatively charged ions such as Cl^- and SO_4^{2-} are repelled from the surface showing generally higher concentrations in the macroporosity. Conversely, cations are attracted, showing enrichment in the microporosity

remains constant throughout the simulation despite changes in ionic strength.

At present, PHREEQC and CrunchFlowMC are the only continuum reactive transport codes that have the capability to simulate reactive transport through a charged clay with explicit treatment of electrostatic effects. Thus, component problems 4 and 5 involve a comparison between those two codes only. Results of component problem 4 are shown in Figs. 8 and 9.

5.5 Main problem: implementation of an EDL and a Stern layer

This scenario uses the same assumptions as component simulation 4, but it includes a Stern layer which compensates for 10 % of the total surface charge of montmorillonite. The remaining 90 % is balanced by the EDL. Species breakthrough curves and the composition of the surface sites on montmorillonite are shown in Figs. 10 and 11, respectively.
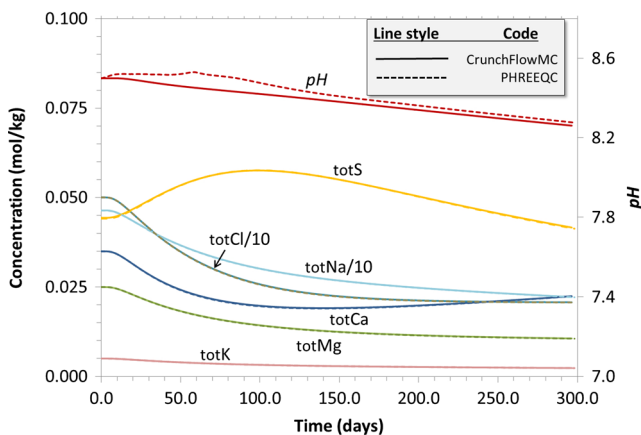
Fig. 10 Results for component problem 5. The composition of the pore water in cell number 25 versus time. Both codes show excellent agreement between breakthrough curves, except for the pH. The relatively strong difference in pH during the transient state of the system appears to be related to differences in the numerical scheme between PHREEQC and CrunchFlowMC
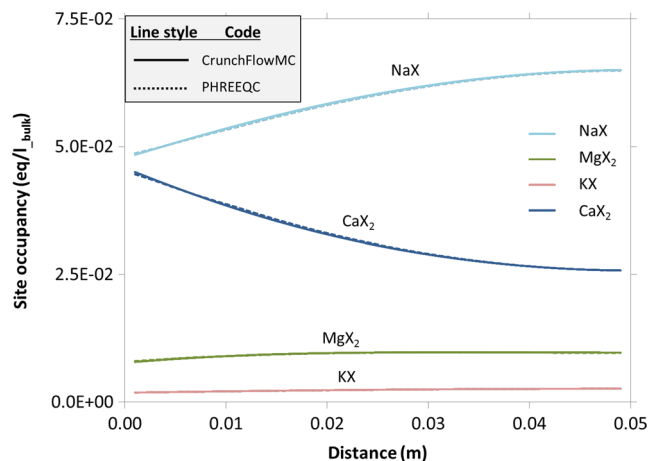
Fig. 11 Spatial profile along the column of the composition of surface complexes on montmorillonite (Stern layer) balancing 10 % of the total charge. The remaining 90 % are balanced by the EDL. The profiles show the preferred uptake of Ca^{2+} onto montmorillonite surfaces in exchange for Na^+, Mg^{2+}, and K^+. Both codes produce the same results

6 Discussion

All codes used in this benchmark, CrunchFlow (Crunch-FlowMC in benchmark problems 4 and 5), MIN3P, FLO-TRAN, and PHREEQC, show excellent agreement between species breakthrough curves for uniform and species-specific diffusion (i.e., a Fickian versus a Nernst-Planck representation of diffusion, respectively) in component problems 1–3 (Figs. 4–7). Note that the quality of agreement between breakthrough curves from different codes is based here solely on visual criteria. To achieve good agreement required certain modifications of the default versions of the codes and/or their thermodynamic databases. These modifications concerned primarily the implementation of consistent activity coefficients and thermodynamic data.

Assessing the difference between a Fickian versus a Nernst-Planck representation of diffusion using Eq. 14 reveals that in simulations with PHREEQC these differences slightly deviate from those computed with the other codes. This is particularly apparent in the SO_4^{2-} profile in Fig. 4, lower panel and in the lower panel of Fig. 6. However, discrepancies between time series amount to less than 1 % which is too small to have any visual impact on the actual species breakthrough curves.

The use of a Fickian versus a Nernst-Planck representation of diffusion results in differences in species concentrations (%D) of less than 8 % (Figs. 4–6). The most significant changes occur during the transient state of the system, that is, upon flushing of the initial pore water. During this transient state, Mg^{2+} shows the largest differences (Figs. 4 and 5, lower panels). While in the case of a single uniform diffusion coefficient, the breakthrough of a species is dependent on the magnitude of the diffusion coefficient and the concentration gradient of the species across the column; in the case of species-specific diffusion, the breakthrough of a species is a function of the diffusion coefficient of the species itself as well as the diffusion coefficients of other charged ions, the magnitude and direction of concentration gradients of all species in the system, and the concentration of that species in solution. Given that Ca^{2+} and Mg^{2+} exhibit similar initial concentration gradients across the inflow boundary, albeit in opposite directions, the much stronger difference between the two diffusion scenarios shown by Mg^{2+} in component problems 1 and 2 appears to be primarily a consequence of the lower absolute concentration of Mg^{2+} in the system. This was confirmed in additional simulations in which the Mg^{2+} concentration was increased while the concentration gradient was maintained, which yielded much smaller differences in the Mg^{2+} concentration in the effluent. Thus, in the case of species-dependent diffusion, as a result of its low concentration, Mg^{2+} shows a relatively strong response to the flux of

species at higher concentrations (e.g., Na^+, Cl^-, or Ca^{2+}) because these species dominate the flux of charge.

In component problem 3, the implementation of exchange reactions leads to the uptake of Ca^{2+} onto the exchanger, promoting the dissolution of gypsum. This results in an inverse relationship between Ca^{2+} and SO_4^{2-} which is controlled by gypsum dissolution and in an inverse relationship between Ca^{2+} on the one hand and Na^+, Mg^{2+}, and K^+ on the other which is controlled by surface reactions (Fig. 6, upper panel; Fig. 7). As the exchange sites become progressively occupied by Ca^{2+}, the concentrations of all exchangeable cations and the SO_4^{2-} concentration never attain steady state during the observation period of 300 days. These transient conditions result in small but prolonged differences between the effluent composition using uniform and species-specific diffusivities (Fig. 6, lower panel).

From the codes used in the benchmark, only PHREEQC and CrunchFlowMC are capable of incorporating an EDL and thus simulate in a physically meaningful way the effect of a negative surface charge of clay surfaces on species transport. The results from both codes of component problems 4 and 5 (Sections 5.4 and 5.5) show excellent agreement, only the time series of the pH shows noticeable differences. In simulations with PHREEQC, we found a relatively strong sensitivity of the pH with regard to the diffusivity assigned to the EDL which we did not encounter in simulations with CrunchFlowMC. However, reducing species diffusivities below those of the benchmark description (Section 3.1) did not have an impact on the computed pH profiles. Furthermore, the pH profiles from PHREEQC and CrunchFlowMC in benchmark problems 4 and 5 and the time series of %D in benchmark problems 1–3 remained unaffected by tightening the convergence criteria and/or increasing the number of time steps. Hence, we suspect the reason for those deviating pH time series to be related to different numerical schemes.

Figure 12 shows the relative timing of the arrival of Cl− and ^2H with and without implementation of an EDL. Without the effect of an EDL (Fig. 12), breakthrough of the half-concentration $0.5 \times (C_{inj} + C_{ini})$ of both species occurs after about 1 pore volume (about 18 days). With the implementation of an EDL (Fig. 12), the relative timing of Cl− and ^2H corresponds to that observed in the experiment (Fig. 2). Upon breakthrough of both species, the composition of the pore water in the free water and the EDL (macro- and the microporosity, respectively) equilibrate. The mass transfer between the relatively small macroporosity and large microporosity causes a retardation of both species compared to the scenario without an EDL. As a result of the negative charge of the montmorillonite surface and the exclusion of anions from the EDL, less mass of Cl− has to be transferred between the two porosity domains until
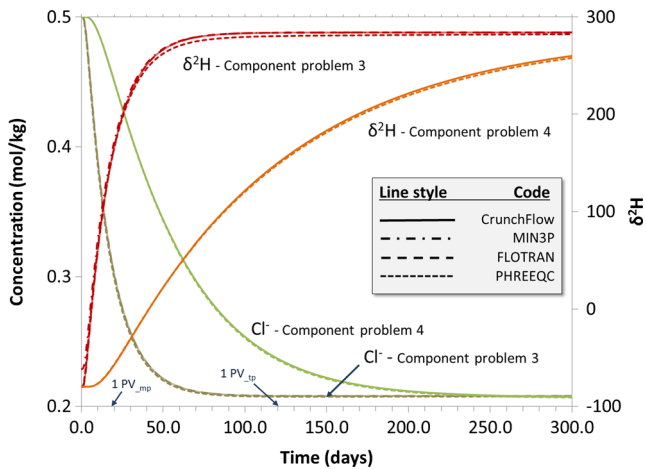
Fig. 12 Comparison of breakthrough curves of Cl and δ^2H for component problems 3 and 4 PV$_{mp}$ and PV$_{1p}$ denote the breakthrough of 1 pore volume for a porosity of 7.1 % (i.e., the porosity in component problems 1-3 and the macroporosity in component problems 4-5) and 47.6 % (the total porosity in component problems 4-5), respectively. Without implementation of an EDL, flushing of Cl contained in the initial pore water and the breakthrough of δ^2H are equally fast, that is, the breakthrough of $0.5 \times (C_{inj} + C_{ini})$ occurs at about 1 pore volume (1 PV$_{mp}$). If the EDL is accounted for, both Cl and δ^2H show a retardation compared to the breakthrough without EDL (*upper panel*). The retardation of δ^2H is more pronounced than that of Cl. The retardation of Cl occurs as Cl contained in the EDL initially, diffuses into the free water upon flushing. Conversely, the breakthrough of δ^2H is slower as it diffuses from the free water into the EDL upon infiltration of the injected fluid

equilibrium is attained. Hence, the breakthrough of Cl$^-$ is faster than that of the deuterium.

Component problems 3, 4, and 5 all reproduce the increase in SO$_4^{2-}$ due to gypsum dissolution, the uptake of Ca^{2+} onto the exchanger combined with the release of Mg^{2+}, K$^+$, and Na$^+$ (Figs. 6, 8, and 10). However, unlike the simulations involving an EDL, "conventional" ion exchange fails to reproduce the process of anion exclusion which was one of the key observations in the bentonite flow-through experiment.

7 Conclusions

The benchmark problems presented here, although complex from a modelling point of view, are still too simple to quantitatively reproduce all aspects of the experiment. For instance, in component problems 4 and 5, we did not include any changes to the Debye length following the infiltration of a dilute solution (Eq. 12), we ignored the porosity changes induced by mineral reaction, we did not consider any effect of the induced pressure gradient and possible compaction of the bentonite sample during the experiment, and we assumed that only the free, charge-balanced water can flow in response to a hydraulic gradient while the water in

the EDL remains immobile. Nevertheless, these simplified models are capable of reproducing most of the observations from the experiment at least in qualitative terms.

It appears that to construct models capable of simulating the transient processes during saturation and compaction of a bentonite barrier requires a combination of pore-scale models that capture the key reactive-transport mechanisms at the microscopic scale and a continuum-scale model that upscales the averaged properties to laboratory (i.e., cm) scale. A model that is predictive at the intermediate scale is a prerequisite for predictive models at the repository scale in the future.

References

1. Pusch, R., Karnland, O., Hökmark, H.: GMM – a general microstructural model for qualitative and quantitative studies of smectite clays. SKB Technical Report 90-43. Swedish Nuclear Fuel and Waste Management Corporation, Stockholm, Sweden (1990)
2. Bolt, G.H., de Haan, F.A.M.: Anion exclusion in soil. In: G.H. Bolt (ed.) Soil Chemistry: B. Physico chemical Models. Elsevier, Amsterdam (1982)
3. Van Loon, L.R., Glaus, M.A., Müller, W.: Anion exclusion effects in compacted bentonites: Towards a better understanding of anion diffusion. Appl. Geochem **22**, 2536–2552 (2007)
4. Tournassat, C., Appelo, C.A.J.: Modelling approaches for anion-exclusion in compacted Na-bentonite. Geochim. Cosmochim. Acta **75**, 3698–3710 (2011)
5. Keller, L.M., Seiphoori, A., Gasser, P., Lucas, F., Holzer, L., Ferrari, A.: The pore structure of compacted and partly saturated MX-80 bentonite at different dry densities. Clays Clay Miner. **62**, 174–187 (2014)
6. Birgersson, M., Karnland, O.: Ion equilibrium between montmorillonite interlayer space and an external solution—consequences for diffusional transport. Geochim. Cosmochim. Acta **73**, 1908–1923 (2009)
7. Parkhurst, D.L., Appelo, C.A.J.: Description of input and examples for PHREEQC Version 3–a computer program for speciation, batch-reaction, one-dimensional transport, and inverse geochemical calculations. http://purl.fdlp.gov/GPO/gpo37078 (2013)
8. Steefel, C.I., Appelo, C.A.J., Arora, B., Jacques, D., Kalbacher, T., Kolditz, O., Lagneau, V., Lichtner, P.C., Mayer, K.U., Meeussen, J.C.L., Molins, S., Moulton, D., Shao, H., Šimůnek, J., Spycher, N., Yabusaki, S.B., Yeh, G.T.: Reactive transport codes for subsurface environmental simulation. Comput. Geosci. doi:10.1007/s10596-014-9443-x (2014)
9. Appelo, C.A.J., Wersin, P.: Multicomponent diffusion modeling in clay systems with application to the diffusion of tritium, iodide, and sodium in opalinus clay. Environ. Sci. Technol. **41**, 5002–5007 (2007)
10. Karnland, O., Olsson, S., Dueck, A., Birgersson, M., Nilsson, U., Hernan-Håkansson, T., Pedersen, K., Nilsson, S., Eriksen, T., Rosborg, B.: Long term test of buffer material at the Äspö hard rock laboratory, LOT project. Final report on the A2 test parcel. TR-09-29, SKB, www.skb.se. Stockholm, Sweden (2009)
11. Fernández, R., Mäder, U., Jenni, A.: Multi-component advective diffusive transport experiment in MX80 compacted bentonite: Method and results of 1st phase of experiment, Nagra Arbeitsbericht, NAB, 11-02. Nagra, Wettingen Switzerland (2011)
12. Mäder, U., Jenni, A., Fernández, R., de Soto, I.: Reactive transport in compacted bentonite: Porosity concepts, experiments and

applications. Goldschmidt Conference Abstracts. (http://www.vmgoldschmidt.org/2012/index.htm) (2012)

13. Steefel, C.I., Maher, K.: Fluid-rock interaction: a reactive transport approach. Rev. Mineral. Geochem. **70**, 485–532 (2009). doi:10.2138/rmg.2009.70.11

14. Mayer, K.U.: MIN3P user guide, University of British Columbia, Department of 413 Earth and Ocean Sciences (2010)

15. Lichtner, P.C.: FLOTRAN Users Manual: Two-phase non-isothermal coupled thermal-hydrologic-chemical (THC) reactive flow and transport code, Version 2. Los Alamos National Laboratory, Los Alamos, New Mexico (2007)

16. Molins, S., Trebotich, D., Steefel, C.I., Shen, C.: An investigation of the effect of pore scale flow on average geochemical reaction rates using direct numerical simulation. Water Resour. Res. **48**, W03527 (2012). doi:10.1029/2011WR011404

17. Liu, C., Shang, J., Zachara, J.M.: Multispecies diffusion models: a study of uranyl species diffusion. Water Resour. Res. **47**, W12514 (2011)

18. Applin, K.R.: The diffusion of dissolved silica in dilute aqueous solution. Geochimica et Cosmochimica Acta **51**(8), 2147–2151 (1987)

19. Li, Y.-H., Gregory, S.: Diffusion of ions in sea water and in deep-sea sediments. Geochimica et Cosmochimica Acta **38**(5), 703–714 (1974)

20. Tournassat, C., Neaman, A., Villieras, F., Bosbach, D., Charlet, L.: Nanomorphology of montmorillonite particles: Estimation of the clay edge sorption site density by low-pressure gas adsorption and AFM observations. Am. Mineral. **88**(11-12), 1989–1995 (2003)

21. Bradbury, M.H., Baeyens, B.: Porewater chemistry in compacted re-saturated MX-80 bentonite. J. Contam. Hydrol. **61**(1-4), 329–338 (2003)

22. Appelo, C.A.J., Van Loon, L.R., Wersin, P.: Multicomponent diffusion of a suite of tracers (HTO, Cl, Br, I, Na, Sr, Cs) in a single sample of opalinus clay. Geochimica Et Cosmochimica Acta **74**, 1201–1219 (2010)